Review of Scientific Instruments

Analysis of the Motional Stark Effect (MSE) diagnostic to measure the rotational transform and current profile in the Large Helical Device

Cite as: Rev. Sci. Instrum. **92**, 053503 (2021); https://doi.org/10.1063/5.0018859
Submitted: 18 June 2020 • Accepted: 07 April 2021 • Published Online: 03 May 2021

M. Sanders, K. Ida, M. Yoshinuma, et al.

Review of Scientific Instruments ARTICLE scitation.org/journal/rsi

Analysis of the Motional Stark Effect (MSE) diagnostic to measure the rotational transform and current profile in the Large Helical Device

Cite as: Rev. Sci. Instrum. 92, 053503 (2021); doi: 10.1063/5.0018859
Submitted: 18 June 2020 • Accepted: 7 April 2021 •
Published Online: 3 May 2021

M. Sanders,[1] K. Ida,[2,3,a)] M. Yoshinuma,[2] C. Suzuki,[2] Y. Yoshimura,[2] R. Seki,[2] M. Emoto,[2] M. Yoshida,[2] and T. Kobayashi[2]

AFFILIATIONS

[1] Department of Applied Physics, Eindhoven University of Technology, Eindhoven 5600 MB, The Netherlands
[2] National Institute for Fusion Science, National Institutes of Natural Sciences, Toki, Gifu 509-5292, Japan
[3] SOKENDAI (The Graduate University for Advanced Studies), Toki, Gifu 509-5292, Japan

[a)] **Author to whom correspondence should be addressed:** ida.katsumi@nifs.ac.jp

ABSTRACT

The analysis method of the Motional Stark Effect (MSE) diagnostic to measure the rotational transform and current profiles in the Large Helical Device has been improved. This was done by using the Variational Moments Equilibrium Code to calculate an equilibrium database for various pressure profiles and current profiles. This method looks for the radial profile of the rotational transform in the equilibrium database that gives the best fit to the polarization angle profiles measured with the MSE diagnostic. This analysis improves the measurements of rotational transform, especially near the magnetic axis, where the sensitivity of the polarization angle measurements becomes low and the uncertainty due to error in the estimation of the Pfirsch–Schlüter current becomes large. The radial profiles of the rotational transform and current profiles for Electron Cyclotron Current Drive and Neutral Beam Current Drive are obtained in the new analysis method with a sufficiently high accuracy to discuss the discrepancy of the current density profiles between the measurements and the calculations.

I. INTRODUCTION

Nuclear fusion is regarded by many as the holy grail of energy production. It offers a practically limitless supply of clean and safe energy, compact power plants, and no climate change driving emissions.[1] However, the realization of a viable nuclear fusion energy plant is still far off as many problems need to be solved.

Magnetohydrodynamics (MHD) instabilities are a big issue in fusion devices, causing a huge increase in heat transport, which leads to heat losses.[2] These instabilities are highly sensitive to the magnetic shear and are especially prevalent near the rational surfaces of the safety factor q, the ratio of toroidal turns per poloidal turn of the flux surface of field lines in the machine. In stellarators, the rotational transform $\iota = 1/q$ is often used. The control of the rotational transform and magnetic shear would be a big step in increasing the stability of nuclear fusion plasmas and indirectly increasing the heating efficiency through better confinement.

The rotational transform in the Large Helical Device (LHD), one of the biggest stellarators in the world, is a superposition of the rotational transform from the toroidal plasma current and that from the current of external coils. Therefore, there are two approaches to control the rotational transform in the LHD. One is control by external coil current and the other is control by altering the plasma current using non-inductive current drive and screening currents. The sign and strength of the magnetic shear have a significant influence on transport and MHD stability, especially near the rational surface. By controlling the radial profile of the toroidal plasma current, the strength of the magnetic shear at the low-order rational surface can be changed. Therefore, the goal of this research is to clarify the role of non-inductive current drive and screening currents in the control of the rotational transform and magnetic shear.

Neutral Beam Current Drive (NBCD) and Electron Cyclotron Current Drive (ECCD) are used to drive current in the LHD. The rotational transform in the plasma core is determined by the

current profile, while the rotational transform at the boundary is determined by the total current, which is measured with Rogowski coils. The Motional Stark Effect (MSE) diagnostic was used to obtain the rotational transform and current profile since Rogowski coils only provide the total current.[3–8] The MSE diagnostic measures the pitch angle of the magnetic field inside the plasma. Using the direction of the magnetic field, the toroidal and poloidal components of the magnetic field can be obtained. These are compared with model data to obtain the rotational transform and magnetic shear. The accuracy of the polarization angle measurements is not high enough to derive the rotational transform near the magnetic axis directly in the LHD. This is because of a lack of MSE measurements in the high field side across the magnetic axis. Because of this, it is difficult to distinguish the vertical magnetic field caused by the plasma current and by the Pfirsch–Schlüter current in the midplane.[9] On top of that, the uncertainty of the Pfirsch–Schlüter current contribution causes a large error bar in the rotational transform near the core of the plasma.[10] These complicating factors need to be taken into account to obtain an accurate measurement for the rotational transform. A large-scale equilibrium database based on the Variational Moments Equilibrium Code (VMEC) calculation for real-time magnetic coordinate mapping has been developed for the LHD.[11] In the analysis of MSE measurements, this VMEC database is used to provide the rotational transform profile during the shot interval (3 min) of LHD experiments.

A new analysis technique for MSE measurements using this VMEC database has been developed in order to provide the precise radial profile of the rotational transform. This new analysis is a hybrid method of two approaches presented in previous papers. One is to select the best fit rotational transform from the VMEC database to reproduce the polarization angle profile measured.[3] The other is to calculate the individual rotational transform values from the individual polarization angle values using the linear relation between the change in the rotational transform and the change in the polarization angle.[10] The details of this hybrid analysis technique are described in this paper.

In Sec. II, the Neutral beam injection (NBI) and ECCD tools are introduced as well as the concept of rotational transform and the MSE diagnostic and its hurdles. In Sec. III, the machine, diagnostics, and actuators used in this MSE experiment are described. In Sec. IV, the improved analysis script is treated, after which the method through which the experiments were performed is given. In Sec. V, the results obtained with the new analysis script are shown. In Sec. VI, a summary is given as well as a proposal for future work.

II. BACKGROUND INFORMATION

A. NBI

Neutral beam injection (NBI) is a versatile tool that can be used for plasma heating, current drive, momentum drive, and fueling. An injected beam needs to consist of neutral particles because ions would be deflected by the high magnetic field. After being injected into the plasma, the particles are ionized again through collisions with particles in the plasma and give off their energy, heating the plasma. In Neutral Beam Current Drive (NBCD), current is driven by creating a difference in the momentum transfer coefficient between the bulk ions and the beam ions, resulting in a higher coulomb collision frequency for the bulk ions than for the beam ions. This is achieved through either a difference in ion charge or a difference in velocity between the ion populations.[12] NBI can be used to heat both electrons and ions depending on the beam energy. However, it has a very broad deposition width. Parallel NBI with a negative ion source is used for NBCD in the LHD.

B. ECCD

In ECCD, the plasma is heated using resonant absorption of electromagnetic waves following the wave particle resonance condition[13]

$$\omega - l\omega_e/\gamma = k_\parallel v_\parallel, \tag{1}$$

where ω is the frequency of the wave, l is the EC wave harmonic number, $\omega_e = eB/m_e c$ is the electron cyclotron gyration frequency, γ is the relativistic factor, and $k_\parallel$ and $v_\parallel$ are the wave number and particle velocity parallel to the magnetic field B, respectively. The high power electromagnetic waves from gyrotrons are redirected and injected into the plasma. The electromagnetic waves deposit their energy to the electrons at the radial position where the resonance condition is met. Through oblique injection of the waves to the magnetic field lines, electrons flowing in one direction along the field line are selectively heated by the waves. The resultant higher momentum leads to a lower collisionality, which causes a longer slowing down time.[12] This, in turn, causes an increase in current. ECCD has a very small deposition width, which makes it ideal for localized current drive. It is also steerable and can be aimed at any flux surface. However, the current drive efficiency is relatively low and the wave frequency tunability is limited.

C. Rotational transform

The safety factor q, the amount of toroidal turns a magnetic field line in a given flux surface makes per poloidal turn, is widely used to evaluate the stability of fusion plasmas. At rational q values, the magnetic field lines are closed, leading to magnetic islands that are often associated with MHD instabilities. The rotational transform, defined as $\iota = 1/q$, is widely used in heliotron and stellarator devices. ι or q is determined using the measured polarization angle γ_p, which is the projection of the magnetic pitch angle of Balmer alpha line emission in the MSE diagnostic. Due to the observation geometry in the machine, changes in the rotational transform are roughly proportional to changes in the measured polarization angle. Due to the geometry of the magnetic field in the toroidal device, changes in the measured polarization angle are smaller, closer to the center for similar changes in the rotational transform. Because of this, the slope $\delta\iota/\delta\gamma_p$ becomes bigger near the center.[10]

D. MSE

MSE polarimetry is a popular way to determine the internal magnetic field of a plasma. It is based on the Stark effect, where an electric field causes a splitting and shift of atomic energy levels in an excited neutral particle. In MSE polarimetry, the motional Stark effect is used, where a Lorentz electric field $E_L = v \times B$ is experienced by particles from the neutral beam moving with a velocity v through a magnetic field B. The emission spectrum from the excited

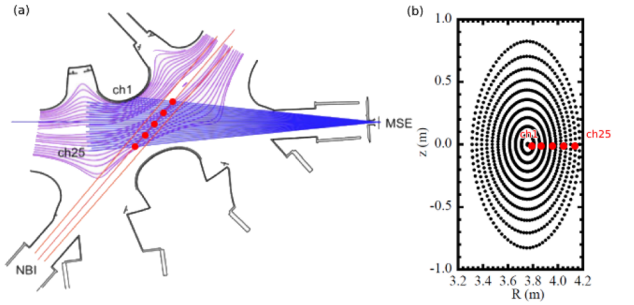

FIG. 1. (a) A top view of the geometry of the MSE diagnostic. The red dots show the intersections of the injected neutral beam and the lines of sight of several diagnostic channels.[10] (b) A plasma with the magnetic axis at a major radius of 3.75 m.[16] (a) was reproduced with permission from Ida *et al.*, Fusion Sci. Technol. **58**, 383–393 (2010). Copyright 2010 AIP Publishing LLC. (b) was reproduced with permission from Ida *et al.*, Nucl. Fusion **45**(5), 391 (2005). Copyright 2005 IAEA.

particles has spectral lines corresponding to the transition energies of the split energy levels. The polarization properties contain linear components and a superposition of circular components, which turn out to be perpendicular to the Lorentz electric field E_L. The polarization angle, which is the projection in the plane of sight of the pitch angle of the magnetic field, can then be used to determine the ratio $\frac{B_{pol}}{B_{tor}}$ between the poloidal magnetic field B_{pol} and the toroidal magnetic field B_{tor}. This can then be used to determine the ratio $\frac{I_{tor}}{B_{tor}}$ between the toroidal current I_{tor} and B_{tor} in the plasma. From there, the rotational transform ι can be obtained. The Balmer alpha line is mostly used for measuring the polarization angle because the Balmer series is the only one in the measurable spectrum and because of the relatively high intensity of the alpha line.[4]

The MSE diagnostic suffers from two big problems that need to be solved before the measurements can be properly analyzed. First is the beam geometry. The NBI probe beam cannot be aimed at the high field side of the plasma due to the beam geometry as seen in Fig. 1. Any passing beam particles would damage the machine. Because of this, the Pfirsch–Schlüter current, a pressure driven current that is already present in the plasma, cannot be evaluated properly. The Pfirsch–Schlüter current creates an offset in the polarization angle measurements, which needs to be properly determined before the measurements can be analyzed.

The second issue is the low sensitivity of the measured polarization angle to the rotational transform near the magnetic axis. The change in the polarization angle for a changing rotational transform becomes small near the plasma center and zero at the magnetic axis. $\frac{\delta\iota}{\delta\gamma_p}$ becomes very high near the plasma center. This means a small measurement error causes a huge error in the calculated rotational transform. The dependency of the rotational transform calculation on $\frac{\delta\iota}{\delta\gamma_p}$ should be reduced as much as possible to enable accurate measurements close to the center.

III. EXPERIMENTAL SETUP

The experiments were performed in the Large Helical Device (LHD), a stellarator type fusion device in Toki, Japan. The device has a major radius R_{ax} of 3.5–4.1 m, an average minor radius of 0.6 m, and a magnetic field of 0.5–3 T. The magnetic axis of plasmas in the device is mostly at 3.6–3.75 m.

The Variational Moments Equilibrium Code (VMEC) model is used to make an equilibrium database containing the rotational transform profile, the major radius of the magnetic axis of the plasma, and the magnetic field profile for a plasma in equilibrium for a given combination of pressure, pressure profile, toroidal current, and current profile.[10,11] It does so by minimizing the energy function[14]

$$W = \iiint_{plasma}\left(\frac{|B|^2}{2\mu_0} + p[\rho]\right)d^3x - \iiint_{vacuum}\frac{|B_v|^2}{2\mu_0}d^3x, \quad (2)$$

where W is the energy, B is the magnetic field in the plasma, B_v is the vacuum magnetic field, μ_0 is the vacuum permeability, p is the pressure, and ρ is the normalized minor radius.

Motional Stark Effect (MSE) measurements were used to obtain the polarization angle required to obtain the rotational transform from the VMEC model. The MSE diagnostic consists of a spectrometer, optical fibers, and four linear polarizers.[10] The polarizers are tilted by 0°, 45°, 90°, and 135° with respect to the horizontal direction. By comparing the difference in light intensity between the perpendicular polarizers, both the linearly polarized π component and the circularly polarized σ component of the light can be obtained. With both, the polarization angle can be obtained by eliminating the circularly polarized component and its overlap with the linearly polarized component. The spectrometer setup is treated in more detail in Ref. 10.

The LHD is equipped with three negative-ion-based NBIs with beam energies of 160–180 keV and two positive-ion-based NBIs with beam energies of 40 keV for hydrogen beams and 60/80 keV for deuterium beams. For a high energy beam, the negative ion sources are used since the neutralization process has a higher cross section, which is essential at high particle energies.[15] One of the negative-ion-based NBIs (NBI No. 3) is used as a probe beam for MSE measurements. They have two ion sources each and are injected tangentially. Of the three negative-ion-based NBIS, the MSE probe and one other are placed in the same direction and another is placed in the opposite direction. By regulating the amount of ion sources per NBI and the total power injected, NBI effects in both directions can be tested. The opposite direction NBI can also be used to cancel out the probe effect in order to minimize the influence of the probe on the experiment.

Electron Cyclotron Resonance Heating (ECRH) is also available in the LHD. Multiple ECRH beams are present. The injection angle of each ECRH beam can be steered two-dimensionally so that the ECRH beams can also be used for ECCD. The magnetic field strength is adjusted to set the resonance layer at the magnetic axis of the plasma for central ECCD.

Although the total toroidal plasma current and the magnetic axis position can be obtained by the Rogowski coils and Thomson scattering, respectively, these measurements are only used for cross-checking and not for the main analysis. This is done in order to avoid the error being influenced by the other diagnostics. Thomson scattering data are only used for the correction for Pfirsch–Schlüter current contributions of the reference shot, which is described in Sec. IV A.

IV. RESEARCH APPROACH

A. Analysis script

A new analysis program was made in python in order to improve the accuracy of measurements of the rotational transform, especially near the center. This was done by taking into account the Pfirsch–Schlüter current offset and by reducing the dependency of the measurements on $\frac{\delta\iota}{\delta\gamma_p}$, which is large at the center due to the geometry of the diagnostic system. The program was uploaded to the NIFS server and integrated into the system.

The program loads data from the server concerning the measured polarization angles and its error, an equilibrium database generated for the shot number using the VMEC and the measured pressure, current, etc. The VMEC generates an equilibrium database with calculated values for the rotational transform, the current profile, the pitch angle, and the polarization angle at the observation point of the MSE diagnostic. It does this for the full parameter space of four parameters; the central pressure P_0, the pressure peaking factor P_{pf}, the total toroidal current I_p, and the current peaking factor I_{pf}. The pressure peaking factor and the current peaking factor determine the shape of the pressure and current profile, respectively, as seen in Tables I and II.

The polarization angle varies significantly along each sight line within the neutral beam diameter and this variation causes a significant wavelength dependence in the polarization angle, which needs to be taken into account in the VMEC calculation. However, the change of the polarization angle, the difference from the polarization angle in the vacuum magnetic field, has almost no wavelength dependence,[3] which confirms that the change in the polarization angle due to the toroidal current does not vary much within the neutral beam diameter. This is because the poloidal field caused by the toroidal current has more or less toroidal symmetry and is constant within the neutral beam width. Therefore, the polarization angle calculated at the beam axis is used in this analysis instead of the polarization angle averaged along the sight line.

Because the Pfirsch–Schlüter current contribution due to the finite pressure in the reference shot is taken into account as $\gamma_{p,cor}$ in this analysis, the zero pressure (i.e., much smaller than the pressure in the target shot) is not a requirement for the reference shot. However, the toroidal current of the reference shot should be as close to zero as possible. The measured polarization angle $\gamma_{p,mes}$ contains a significant offset due to the Faraday rotation from the windows in the magnetic field, which depends on the configuration and strength of the magnetic field. In order to subtract the offset due to the Faraday rotation effect, measurements of the polarization angle of the reference shot are necessary for MSE measurements. Ideally, the reference shot has a current and pressure of 0. In this analysis method, the difference between the measured and the calculated change in the polarization angle resulting from the current and pressure profile, $\gamma_{p,diff}$ and $\gamma_{p,cal}$, respectively, is minimized to determine the rotational transform rather than using the absolute value of the polarization angle.

In the previous analysis, $\gamma_{p,diff} = \gamma_{p,mes} - \gamma_{p,ref}$ and $\gamma_{p,cal} = \gamma_{p,VMEC} - \gamma_{p,vac}$, where $\gamma_{p,ref}$ is the measured polarization angle from the reference shot, $\gamma_{p,VMEC}$ is the polarization angle calculated by the VMEC for a set of parameters, and $\gamma_{p,vac}$ is the polarization angle calculated by the VMEC for a vacuum shot. Here, it was assumed that the reference shot has zero current and zero pressure (zero Pfirsch–Schlüter current). In the new analysis, the procedure uses $\gamma_{p,diff} = \gamma_{p,mes} - \gamma_{p,ref} + \gamma_{p,cor}$ and $\gamma_{p,cal} = \gamma_{p,VMEC} - \gamma_{p,vac}$, where $\gamma_{p,cor}$ is the Pfirsch–Schlüter current contribution of the reference shot defined as $\gamma_{p,cor} = \gamma_{p,VMEC(ref)} - \gamma_{p,vac}$ by assuming the reference shot has zero current but finite plasma pressure. The difference in the polarization angle of the reference shot is caused by only Pfirsch–Schlüter currents and can be calculated from the central pressure P_0 and pressure peaking factor P_{pf} that give the shift of magnetic axis consistent with the measurements. Therefore, $\gamma_{p,cor}$ is calculated from the shift of the magnetic axis of the reference shot evaluated by the temperature profile measured with YAG Thomson scattering. However, the central pressure P_0 and pressure peaking factor P_{pf} of the target plasma are selected from the data that give the best fit to the measured polarization angle profile.

For each of the parameter sets from the VMEC database, the calculated polarization angle $\gamma_{p,VMEC}$ in equilibrium is taken. By comparing the expected polarization angle for each equilibrium state

TABLE I. The pressure profile for the normalized minor radius $\rho = r_{eff}/a_{99}$ and the central pressure P_0 for different values of the pressure peaking factor P_{pf}.[11] Reproduced with permission from Suzuki *et al.*, Plasma Phys. Controlled Fusion **55**, 014016 (2012). Copyright 2012 IOP Publishing Ltd. All rights reserved.

Pressure profile	P_{pf}
$P_0(1-\rho^8)^2$	1.41
$P_0(1-\rho^8)(1-\rho)$	2.14
$P_0(1-\rho^2)^2$	3.00
$P_0(1-\rho^2)^3$	4.00
$P_0(1-\rho^2)^4$	5.00

TABLE II. The current profile for the normalized minor radius $\rho = r_{eff}/a_{99}$ for different values of the current peaking factor I_{pf}.

Current profile	I_{pf}
$(1-\rho^2)^9$	10.0
$(1-\rho^2)^8$	9.0
$(1-\rho^2)^7$	8.0
$(1-\rho^2)^6$	7.0
$(1-\rho^2)^5$	6.0
$(1-\rho^2)^4$	5.0
$(1-\rho^2)^3$	4.0
$(1-\rho^2)^2$	3.0
$(1-\rho^2)$	2.0
$(1-\rho^8)^2$	1.41
$(1-\rho^8)^2 - 0.6(1-\rho^2)^3$	0.71
$(1-\rho^8)^2 - 0.9(1-\rho^2)^3$	0.21
$(1-\rho^8)^2 - 1.2(1-\rho^2)^3$	−0.49
$(1-\rho^8)^2 - 1.5(1-\rho^2)^3$	−1.49
$(1-\rho^8)^2 - 1.8(1-\rho^2)^3$	−3.06
$(1-\rho^8)^2 - 2.1(1-\rho^2)^3$	−5.91
$(1-\rho^8)^2 - 2.4(1-\rho^2)^3$	−12.6

in the parameter space $[P_0, P_{pf}, I_p, I_{pf}]$ and the experimentally measured polarization angle, the most likely state of the plasma can be deduced. This comparison is done through a calculation of χ, which is calculated by

$$\chi[t, P_0, P_{pf}, I_p, I_{pf}] = \frac{1}{N}\sum_{i=1}^{N}\left(\frac{\gamma_{p,diff}[t,\rho_i] - \gamma_{p,calc}[P_0, P_p, I_p, I_{pf}, \rho_i]}{\gamma_{p,error}[t,\rho_i]}\right)^2, \quad (3)$$

where χ is evaluated for the time t, N is the amount of data points in the radial dimension, i is the radial index, and $\gamma_{p,error}$ is the measurement error of $\gamma_{p,mes}$. The minimum value for χ gives the equilibrium state in the database that fits best to the measured data. The division by $\gamma_{p,error}$ is done so that the accurate measurements with a low error have a higher weight in finding the minimum of χ. Taking the equilibrium state in the database with the lowest value of χ, the radial profile of the rotational transform $\iota_{bestfit}$ and the polarization angle $\gamma_{p,bestfit}$ with the best fit to the experimental data are obtained.

Examples of χ plots are shown in Fig. 2. The sensitivity of χ to the current peaking factor is higher than the sensitivity of χ to the total toroidal current. Since the beam has a significant contribution to the pressure, especially at the low density, the Thomson scattering diagnostic fails to provide an accurate value for the central pressure P_0. As seen in Figs. 2(a) and 2(b), the sensitivity of χ to the central pressure is not as high as the sensitivity to the current peaking factor but still higher than the sensitivity to the total toroidal current. Since the χ value is quite insensitive to the pressure peaking factor as seen in Fig. 2(c), the pressure peaking factor can be preset to a constant value near the measured value to reduce the computing time of the analysis. The Rogowski coil measurements are only used to determine the sign of the toroidal current and check whether the fitted values of I_p and I_{pf} are reasonable. The program only looks for the minimum of χ in the dimension space where the sign of the current density corresponds to that of the measured value.

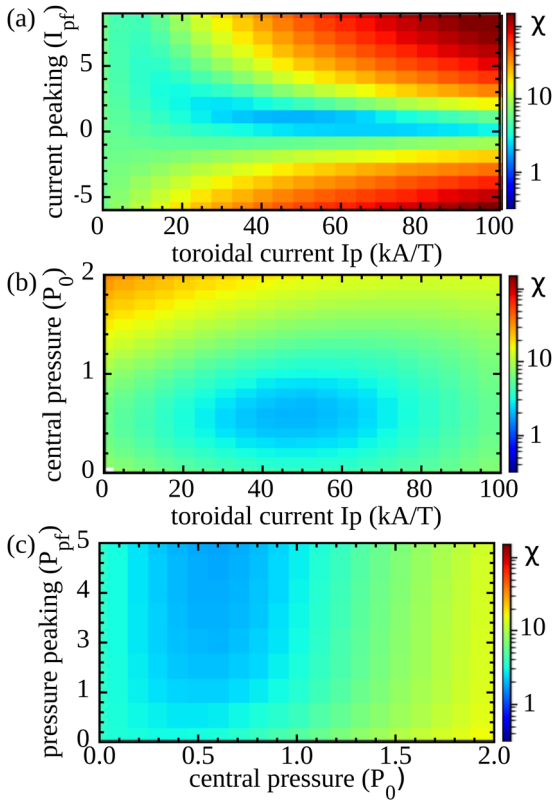

FIG. 2. Examples of calculated χ values in the parameter space of (a) the toroidal current and the current peaking factor ($I_p$andI_{pf}), (b) the toroidal current and the central pressure ($I_p$andP_0), and (c) the central pressure and pressure peaking factor (P_0andP_{pf}). The calculations are given at t = 2.3 s for shot number 82 716.

Figure 3 shows the radial profile of the measured polarization angle and the calculated polarization angle, which has the best fit to the measured values. The correction due to the Pfirsch–Schlüter current contribution of the reference shot (the differences between the two measured polarization angles) increases toward the plasma center and reaches 1° at the plasma center $r_{eff}/a_{99} = 0$. The radial profile of the polarization angle reproduced by the pressure and current profiles in the database is consistent with the measured polarization angle within the error bar. Therefore, the variation of the pressure and current profiles shown in Tables I and II in the database is sufficient for this measurement.

Before, the rotational transform profile was calculated by[3,10]

$$\iota[t,\rho] = \iota_{vacuum} + \frac{\delta\iota}{\delta\gamma_p}[t,\rho](\gamma_{p,mes} - \gamma_{p,vacuum}), \quad (4)$$

where ι_{vacuum} and γ_{vacuum} are the rotational transform and polarization angle of the vacuum case in the database, respectively, and $\delta\iota/\delta\gamma_p$ is calculated for each point in the radial direction based on multiple values in the parameter space of the VMEC database at that radial position. Because $\delta\iota/\delta\gamma_p$ becomes very large near the magnetic axis of the plasma,[10] the error becomes very large for large differences between $\gamma_{p,mes}$ and $\gamma_{p,vacuum}$.

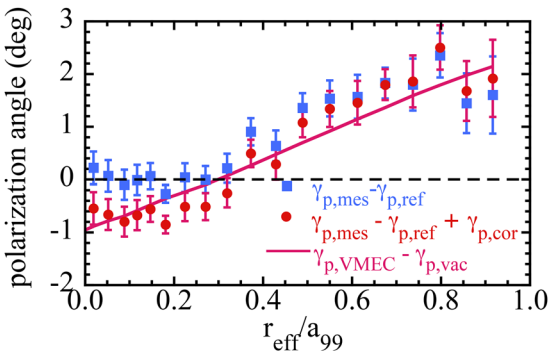

FIG. 3. The radial profiles of the polarization angle measured with (red) and without (blue) the correction for the Pfirsch–Schlüter current contribution of the reference shot are given. The radial profile of the polarization angle calculated with the VMEC (solid line), which has the best fit to the measured values with correction, is given in red. The measurements are given at t = 2.3 s for shot number 82 716.

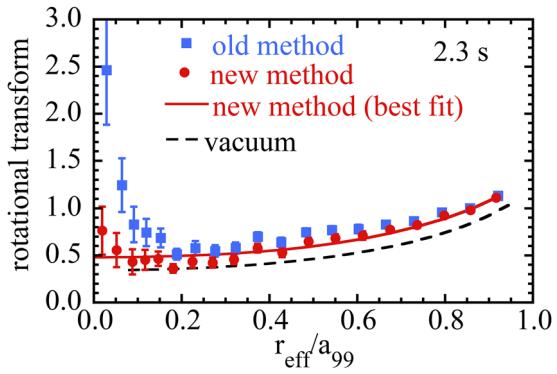

FIG. 4. The radial profiles of the measured rotational transform for both the old and new methods for shot 82 716 at t = 2.3 s. The radial profile of the best fit VMEC equilibrium rotational transform determined with the new method is plotted in a red curve. The rotational transform profile in the vacuum field calculated with the VMEC is plotted with a dashed line. The plotted error bars of the rotational transform are calculated as $\iota_{error} = \gamma_{p,error} \cdot \delta\iota/\delta\gamma_p$.

In the new analysis method, individual ι values are calculated as

$$\iota[t,\rho] = \iota_{bestfit} + \frac{\delta\iota}{\delta\gamma_p}(\gamma_{p,mes} - \gamma_{p,bestfit}), \tag{5}$$

where $\iota_{bestfit}$ is the rotational transform for the equilibrium state in the VMEC database with the lowest χ value. This method provides a ι profile that takes into account the entire radial profile of the polarization angle and always satisfies the equilibrium conditions, making unrealistic results less common. $\delta\iota/\delta\gamma_p$, which becomes very large near the center, no longer contributes to the final result. The difference between the methods is shown in Fig. 4. The old method starts to diverge heavily near the center, while the new method gives much less divergence and the deviation from the best fit VMEC equilibrium iota (red curve) is relatively small even near the magnetic axis. Here, the error bars of the rotational transform are evaluated from the relative error bars of the polarization angle. The uncertainty of the polarization angle introduced by the evaluation of the Pfirsch–Schlüter current is not included in these error bars. The contribution of the Pfirsch–Schlüter current to the polarization angle compared to the contribution by the toroidal current increases sharply toward the plasma center. Even a small uncertainty in the polarization angle due to the Pfirsch–Schlüter current contribution causes a large uncertainty in the rotational transform because of the large $\delta\iota/\delta\gamma_p$ near the plasma center. In the old method, the values of the rotational transform become unrealistic due to the incorrect assumption that the Pfirsch–Schlüter current would be zero in the reference shot. In the new method, the Pfirsch–Schlüter current contribution of the reference shot is evaluated correctly and the values of the rotational transform become more realistic.

For every one of the four parameters (P_0, P_{pf}, I_p, and I_{pf}), a three-point polynomial fit was made to find a better resolution for the minimum χ. Taking the other three parameters as a constant at the found values, a second order polynomial was made for the three χ values at the found parameter value and two neighbors in the database. By calculating the minima of these polynomials, a higher resolution was achieved for the values of each of the four parameters at minimum χ. The higher resolution parameters values are then used to calculate a new ι value through a linear interpolation of the ι values in the database mesh. This interpolation process improves the accuracy of $\iota_{bestfit}$ even in the course mesh of the VMEC database.

To better look at the effects of the currents, the current profile was calculated from the total toroidal current and the current peaking factor using the formulas given in Table II. The current density profile is currently only known for a specific set of current peaking factors rather than the full range. The equations are currently implemented specifically for each case throughout the known I_{pf} range and needs to be automized before the script can handle flexible ranges. As it is, it calculates the difference between the measured value of the current peaking factor and two states in the VMEC database with neighboring I_{pf} values for which the current density profile is known. It then takes a weighted average as the current density profile.

The difference between the old method and the new method is summarized in Table III. While the central pressure, P_0, pressure peaking factor, P_{pf}, and toroidal current, I_p, are determined by the Thomson scattering diagnostic and Rogowski coil measurements in the old method, the P_0, P_{pf}, and I_p values that give the minimum χ are selected from a VMEC database in the new method. Because of that, the main analysis of the MSE diagnostic becomes independent of other diagnostics and the error of the rotational transform

TABLE III. An overview of the differences between the old method and the new method for analysis of the MSE diagnostic data.

	Old method[3,10]	New method
P_0	Determined by Thomson scattering	Selected from the VMEC database (11 values)
P_0 reference shot	Assumed to be zero	Determined by Thomson scattering
P_{pf}	Determined by Thomson scattering	Selected from the VMEC database (5 values) or preset
P_{pf} reference shot	Not necessary because $P_0 = 0$	Determined by Thomson scattering
I_p	Determined by Rogowski coils	Selected from the VMEC database (13 values)
Sign of I_p	Determined by Rogowski coils	Determined by Rogowski coils
I_{pf}	Selected from the VMEC database (11 values)	Selected from the VMEC database (17 values)
Polarization angle	$\gamma_{p,dif} = \gamma_{p,mes} - \gamma_{p,ref}$	$\gamma_{p,dif} = \gamma_{p,mes} - \gamma_{p,ref} + \gamma_{p,cor}$
Individual ι values	$\iota = \iota_{vac} + \delta\iota/\delta\gamma_p(\gamma_{p,mes} - \gamma_{p,vac})$	$\iota = \iota_{bestfit} + \delta\iota/\delta\gamma_p(\gamma_{p,mes} - \gamma_{p,bestfit})$
Output	Best fit ι curve[3] OR 1 data point[10]	Best fit ι curve AND ι data point

becomes free of the uncertainty of Thomson scattering diagnostic and Rogowski coil measurements. The Thomson scattering diagnostic is used only to determine the central pressure P_0 and the pressure peaking factor P_{pf} of the reference shot, and Rogowski coil measurements are used only to determine the sign of the toroidal current I_p. The database of the current peaking factor included only 11 profiles in the old method and the database is expanded to 17 profiles by including more peaked profiles in the new method. Due to the addition of the other parameters, the total number of equilibrium states in the database for searching the minimum χ is 12 155 for a full scan and 2431 for a preset value of P_{pf} in the new method, while it was only 11 in the old method. A large number of equilibrium states in the database contributes to improving the accuracy of the rotational transform profile in the MSE measurements. The pressure and Pfirsch–Schlüter currents of the reference shot were assumed to be zero in the old method, but in the new method, the central pressure of the reference shot is evaluated from the Thomson scattering diagnostic measurements and the change in the polarization angle due to the Pfirsch–Schlüter currents of the reference shot has been taken into account in the form of a correction to the polarization angle, $\gamma_{p,cor}$. The individual values of the rotational transform ι are calculated through linear interpolation of the best fit rotational transform in the new method, while it was calculated from the rotational transform in the vacuum field in the old method. This change improves the accuracy of the calculation of individual values of the rotational transform.

B. Experimental method

The effect of an NBCD direction switch on the behavior of the plasma is tested. Shots with a switch in the NBI direction are compared to similar shots with a constant direction. Due to the abnormally big change in non-inductive current, the screening current is expected to be very high.

The difference between NBCD and ECCD is also tested. The ECCD setup is always aimed at the magnetic axis, so NBCD shots aimed at the axis are best for this study. The difference in current drive efficiency, time scales, and screening current are studied. The effect of these three things on the current profile is then translated to the effect on the rotational transform.

MSE shots with long pulse discharges, low density, and high NBCD current are desirable for this study. Long pulse discharges show a good representation of the plasma behavior in time. NBCD and ECCD drive a high current in low density plasmas. It will also cause less absorption of the NBI power for the MSE probe beam, making for a higher beam intensity inside the plasma, which leads to a stronger signal. High NBCD currents mean that the background currents like the Pfirsch–Schlüter current have less of an impact, which increases the accuracy of the measurements.

A reference shot is taken for each measurement in order to measure the polarization angle resulting from the magnetic field caused by the external coils. This reference shot has a discharge with low plasma density, two low power NBIs in the opposite direction so that as little as possible net toroidal current is driven and the same magnetic configuration and beam energy as the probe beam used in the actual measurement.

The expectation is that NBCD in the co-direction will increase the rotational transform at the injection radius just after it has been turned on due to non-inductive current drive, while the screening current around the injection radius will decrease the rotational transform. The opposite counts for counter-direction NBI. The ECCD has a smaller beam size, so the effect is expected to be more localized. For off-axis current drive, the center is expected to experience more screening current because it has a higher temperature, which leads to a higher conductivity.

V. RESULTS

There are three issues for which to test the new analysis method. First is the difference between co-direction and counter-direction ECCD measurements. Second is the difference between ECCD and NBCD measurements. Third is the difference in behavior between NBCD with a constant beam direction and NBCD with a switch in the beam direction halfway. The main concern in these initial measurements is whether the new analysis method is able to discern the different behaviors near the center with a high enough accuracy. All experiments were done for plasmas with the magnetic axis at 3.75 m and a toroidal magnetic field in the negative direction of 1.3–1.4 T. In the discharges 147 317 and 147 324 (3.75 m, 1.375 T), the 77 GHz ECCD setup was aimed at the magnetic axis for on-axis heating. However, in discharge 82 716 (3.75 m, 1.3 T), the frequencies of the gyrotrons used were 84 GHz (0.15–0.65 s) and 82.7 GHz (3.8–4.3 s). Although the resonance layer of 77 GHz ECH is located at the magnetic axis in the plasma with the magnetic field of 1.375 T, there is no resonance layer of 84 GHz ECH near the magnetic axis in the plasma with the magnetic field of 1.3 T. The ECRH beams are aimed at the innermost resonance layer, which is apart from the magnetic axis for ECRH (not for ECCD). The deposition locations of those 84 GHz or 82.7 GHz ECRH beams are $\rho \sim 0.45$. All the currents were normalized to the toroidal magnetic field because different B_{tor} values were used during the experiments and because the rotational transform depends on I_{tor}/B_{tor}.

ECCD is expected to be more localized than NBCD as the power deposition width calculated using the ray tracing code LHDGauss is $\sim 0.2a$,[17] while the NBI deposition width calculated using the FIT3D code is $\sim 0.6a$.[18] ECCD is also aimed at the center, while NBCD has a tangential injection radius at 3.7 m, where a lot of the absorption happens even more outward. NBCD is expected to cause a gradual increase or decrease near the injection radius until saturation. Right after turning it on or switching direction, a transient current in the opposite direction is expected due to screening current. Any positive current is expected to cause the local ι above the vacuum level, while a negative current is expected to cause it to go below the vacuum level.

A. ECCD

First, the difference between the co-direction and counter-direction ECCD is treated. As seen in Fig. 5, the three NBI beams are made to be nearly balanced so as to almost cancel each other out. This way, the current drive by NBI is minimized so that the main contribution to the current drive is from the ECCD. The co-direction and counter-direction case have the same inputted ECCD power. The probe NBI (No. 3) is injected 2.3 s after the ECCD power is turned on for MSE measurements.

Figures 6 and 7 show the current density profiles for co- and counter-current ECCD against the normalized effective minor

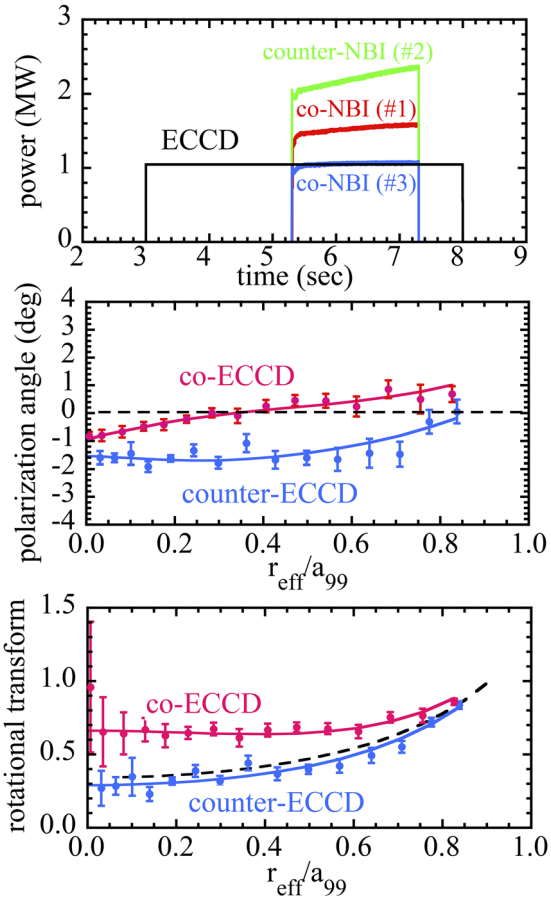

FIG. 5. The time evolution of the three NBIs (two co-NBIs and one counter-NBI) and ECCD power for shot numbers 147 317 and 147 234 (same waveform). The co-NBI (No. 3) is used as a probe beam for the MSE measurements. The radial profiles of the polarization angle and the rotational transform at t = 6.4 s are plotted for co-ECCD (shot 147 317) and counter-ECCD (shot 147 324).

radius r_{eff}/a_{99}, where r_{eff} is the effective minor radius with regard to the magnetic axis and a_{99} is the effective minor radius where 99% of the kinetic energy of the plasma is confined. The figures show a peaked profile at the center with very little difference over time. A difference in peaking factor is seen between the two cases, where the co-current case has a peak current density around 100 kA/T/m^2, while the counter-current case has a peak current density around 60 kA/T/m^2. This behavior can be seen throughout the entire dataset as seen in Fig. 8. This agrees with calculations done using the TRAVIS ray tracing code,[19] which shows a deposition closer to the axis for co-direction ECCD as seen in Fig. 9.

Figures 6 and 7 also show the expected behavior in the rotational transform where Fig. 6 shows an ι well above the vacuum profile within the error bar boundaries and Fig. 7 shows ι under it. Here, the error bar calculated from the errors in the polarization angles is plotted. As seen in Fig. 4, these error bars are comparable to the deviations of the iota values from the best fit VMEC equilibrium iota curve, which confirms that the variation of equilibrium iota profiles is sufficient for these measurements. If the deviations

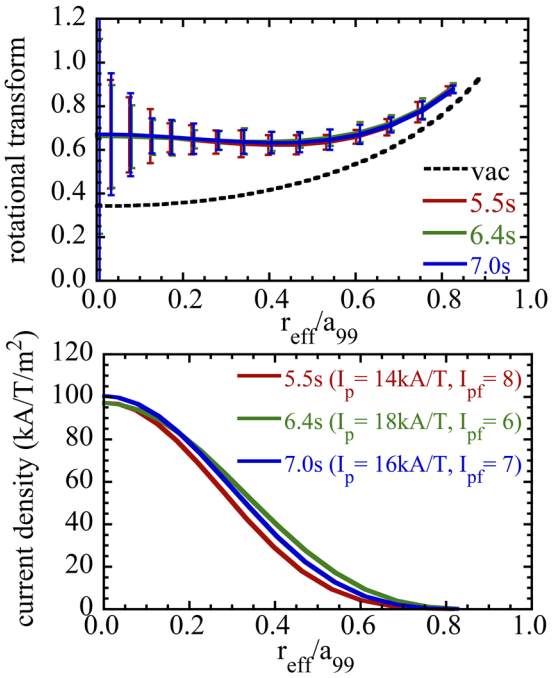

FIG. 6. The radial profiles of the rotational transform and current density at 5.5, 6.4, and 7.0 s for shot number 147 317 measured using the MSE diagnostic for co-ECCD.

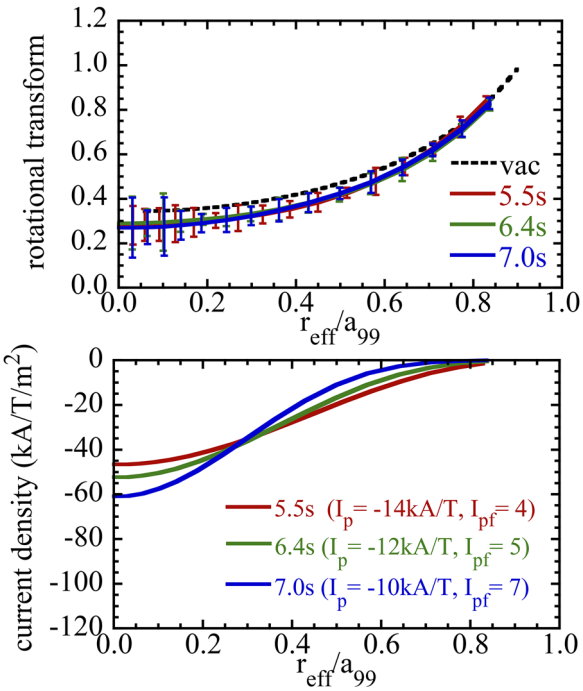

FIG. 7. The radial profiles of the rotational transform and current density at 5.5, 6.4, and 7.0 s for shot number 147 324 measured using the MSE diagnostic for counter-ECCD.

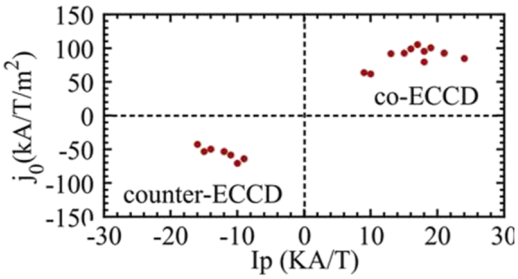

FIG. 8. The measured peak current density plotted against the measured total current for measurements of shot numbers 147 317–147 328. Both ECCD shots in the co-direction and in the counter-direction are shown.

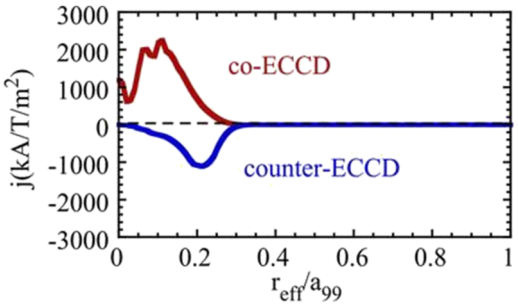

FIG. 9. The expected current density as a result of ECCD as a function of the effective normalized minor radius calculated using the ray-tracing code TRAVIS for shot numbers 147 317 and 147 324.

would significantly exceed the error bars, it would be a sign that the variation of the equilibrium iota profiles is insufficient. The measured current profiles shown in Figs. 6 and 7 are broader than the current profiles estimated by the TRAVIS ray-tracing code shown in Fig. 9. The TRAVIS code provides the current density profile in the steady-state where the screening current becomes zero. In contrast, the total current plasma increases in time in the ECCD discharge, which indicates that the current density profile does not reach the steady-state phase. Therefore, there should be a significant effect of screening current in the measured current density in this experiment. This would be one of the reasons for the discrepancy between the simulation and the measurements.

B. NBCD

Figure 10 shows the change in the polarization angle profile and the rotational transform profile in a discharge where the direction of the neutral beam is switched from the co-direction (No. 1) to the counter-direction (No. 2) with a continuous probe beam (No. 3) for MSE measurements. The polarization angle in the core decreases at the beginning of co-NBI (t = 1.1 s) but then gradually increases due to the non-inductive current by co-NBI (NBCD). The rotational transform is close to the vacuum at the onset (t = 0.5 s). When the co-NBI is injected into the plasma early on, the rotational transform near the plasma edge starts to increase in the direction of the non-inductive current drive due to the low electron temperature. However, when the screening current due to the toroidal electric

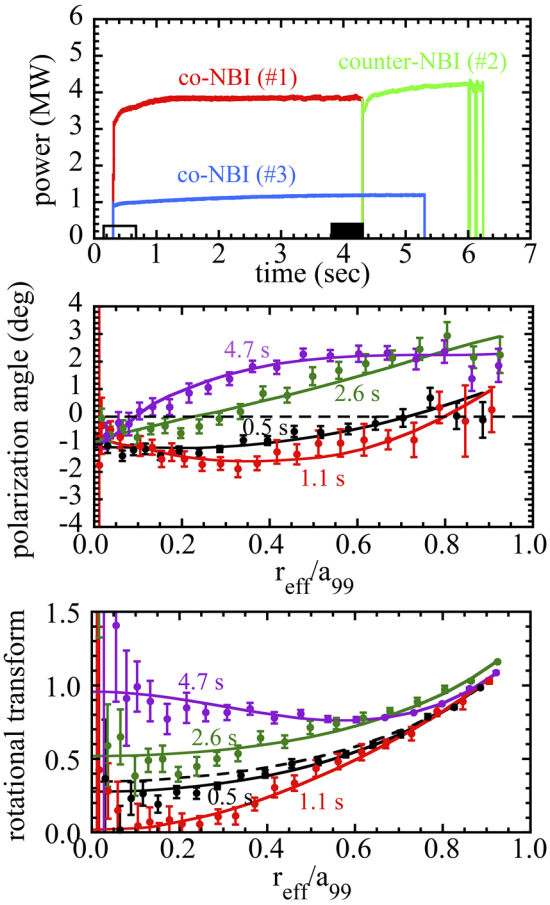

FIG. 10. The time evolution of the three NBIs (two co-NBIs and one counter-NBI) and ECCD power for shot number 82 716. The co-NBI (No. 3) is used as a probe beam for the MSE measurements. The radial profiles of the polarization angle and the rotational transform at 0.5, 1.1, 2.6, and 4.7 s are plotted. The direction of the NBCD is switched at t = 4.3 s from the co-direction to the counter-direction.

field driven by the edge $\delta I/\delta t$ is equal to the non-inductive current, the rotational transform near the plasma center does not increase. In a tokamak, the screening current is generally smaller than the non-inductive current. In the LHD, this current can be even larger than the non-inductive current. Due to the transient negative current just after the start of the co-NBI pulse, the rotational transform near the plasma center decreases transiently and drops close to zero as observed in the radial profile of the rotational transform at 1.1 s. Then, the core rotational transform increases over time and eventually becomes larger than the vacuum rotational transform (dashed line) during the co-NBI (t = 0.3–4.3 s) phase. When co-direction NBI is switched to the counter-direction, the rotational transform near the plasma center increases due to the transient positive current.[20] This positive current is clearly observed at 4.7 s in Fig. 12 and also predicted by calculations done using the TASK3D code.[10]

Figure 11 shows the expected energy deposition of the NBI calculated using the FIT3D code. As seen in Fig. 12, the current is located a lot more toward the center of the plasma. A gradual

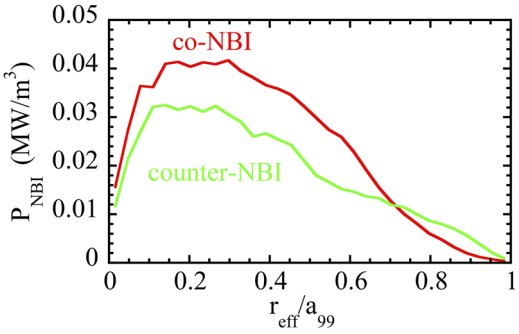

FIG. 11. The radial profiles of the deposition power calculated with the FIT3D code for both co- and counter NBIs with 1 MW of heating power.

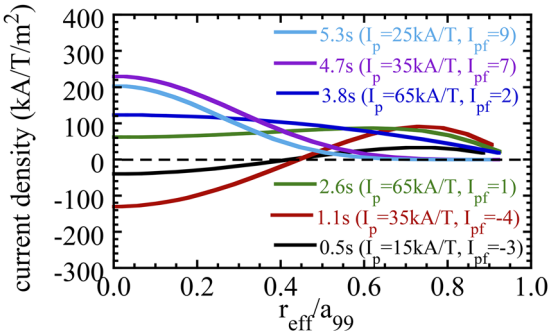

FIG. 12. The radial profile of the current density at 0.5, 1.1, 2.6, 3.8, 4.7, and 5.3 s for shot number 82 716 measured using the MSE diagnostic.

increase in the current density near the injection radius is observed near the injection radius $r_{eff}/a_{99} = 0.2$. After the onset at t = 0.5 s, the central toroidal current decreases from zero to a negative current as seen in time slices at t = 0.5 and t = 1.1 s, while the edge toroidal current increases. Since no significant ECCD is expected in shot 82 716, the negative current in the core region is a screening current. A steady rise in current over time is seen in the region where energy deposition is expected. At 2.6 s, the outer current density has not increased much, whereas the central current density has risen considerably. Over time, the central current keeps steadily rising. The same behavior is observed in the rotational transforms seen in Fig. 10.

The co-direction NBCD is switched to counter-direction NBCD just after 4.3 s. Then, right after the switch, the current density in the outer region of the plasma is pushed down by the direct current drive, while the current density in the center of the plasma ($r_{eff}/a_{99} < 0.2$) increases likely due to the screening current. After the outer current has stabilized, we see a slight decrease in the central current density at 5.3 s where the total current is reduced by the NBCD.

VI. CONCLUSION

A program was developed to improve the MSE spectrometry analysis method. The accuracy was increased by subtracting the calculated polarization angle for finite pressure reference shots from the measured polarization angle to take the Pfirsch–Schlüter current into account. The high impact of $\frac{\delta\iota}{\delta\gamma_p}$, especially near the magnetic axis, was reduced by using a precalculated ι value from the VMEC database and using that as the baseline instead of the vacuum ι. This improved analysis method made it possible to see the expected behavior of NBCD and ECCD near the magnetic axis of the plasma for the first time. A difference in peaking for co-direction current drive and counter-direction current drive could be recognized. A significant impact of screening current near the axis for NBCD was also recognized after switching the direction of the beam.

The total plasma current I_p can be measured from the polarization angle at the plasma edge ($r_{eff}/a_{99} = 1$). However, there is no channel for the polarization angle measurements at the plasma edge and the total plasma current is evaluated by extrapolation of the measured polarization angle. The error bar of the polarization angle becomes larger near the plasma edge ($r_{eff}/a_{99} > 0.8$). The measurements of the total plasma current are less accurate than the measurements of current density and rotational transform in the core region. Therefore, the precise measurement of the current density profile is not obtained due to a lack of MSE measurements near the plasma edge although the measurement of the rotational transform in the core region is accurate enough to discuss the magnetic shear in the core region.

For future work on the analysis program, a full error analysis should be done. The current density should have a more generally applicable calculation. As it is, it can only calculate the density profile for a manually inserted range of peaking profile factors in which it can interpolate but not extrapolate. The current density should also have an error bar to give better insight into the quality of the data. While the method shows the ability to see temporal changes, more data are needed in order to quantify any effects of the current drive, screen currents, and current diffusion on the rotational transform. More shots comparing the NBCD vs ECCD and continuous beam vs direction switch are needed, especially near the start of current drive. Apart from that, the dependence of the effects of NBCD and ECCD on the radial position of the magnetic axis of the plasma could be studied to determine current drive efficiency. The impact of short ECCD pulses could be tested to see whether the screening current cancels out the non-inductive current and only the peaking factor changes or whether the total toroidal current increases even at short pulses.

The improved analysis technique has been used for precise measurements of the radial profile of the rotational transform to obtain a better understanding of MHD instabilities.[21,22]

ACKNOWLEDGMENTS

The authors are grateful to the technical staff of the LHD for their excellent support of this work. This work was supported by the National Institute for Fusion Science grant administrative budgets (Grant Nos. NIFS10ULHH021 and NIFS17KLPH030) and JSPS KAKENHI Grant Nos. JP15H02336, JP16H02442, and JP17H01368.

DATA AVAILABILITY

The data that support the findings of this study are available from the corresponding author upon reasonable request.

REFERENCES

[1] C. L. Smith and S. Cowley, Philos. Trans. R. Soc., A **368**(1914), 1091 (2010).
[2] H. J. de Blank, Fusion Sci. Technol. **53**(2T), 59 (2008).
[3] K. Ida, M. Yoshinuma, K. Y. Watanabe, T. Kobuchi, and K. Nagaoka, Rev. Sci. Instrum. **76**, 053505 (2005).
[4] R. C. Wolf, A. Bock, O. P. Ford, R. Reimer, A. Burckhart, A. Dinklage, J. Hobirk, J. Howard, M. Reich, and J. Stober, J. Instrum. **10**(10), P10008 (2015).
[5] F. M. Levinton, R. J. Fonck, G. M. Gammel, R. KaIta, H. W. Kugel, E. T. Powell, and D. W. Roberts, Phys. Rev. Lett. **63**(19), 2060 (1989).
[6] F. M. Levinton, G. M. Gammel, R. Kaita, H. W. Kugel, and D. W. Roberts, Rev. Sci. Instrum. **61**(10), 2914 (1990).
[7] F. M. Levinton, Rev. Sci. Instrum. **63**(10), 5157 (1992).
[8] D. Wróblewski and L. Lao, Rev. Sci. Instrum. **63**(10), 5140 (1992).
[9] T. J. Dobbins, K. Ida, C. Suzuki, M. Yoshinuma, T. Kobayashi, Y. Suzuki, and M. Yoshida, Rev. Sci. Instrum. **88**, 093518 (2017).
[10] K. Ida, M. Yoshinuma, C. Suzuki, T. Kobuchi, K. Y. Watanabe, and LHD Experiment Group, Fusion Sci. Technol. **58**, 383–393 (2010).
[11] C. Suzuki, K. Ida, Y. Suzuki, M. Yoshida, M. Emoto, and M. Yokoyama, Plasma Phys. Controlled Fusion **55**, 014016 (2012).
[12] E. Westerhof, Fusion Sci. Technol. **57**(2T), 92 (2010).
[13] E. Ott, B. Hui, and K. R. Chu, Phys. Fluids **23**, 1031 (1980).
[14] A. Kleiner, J. P. Graves, W. A. Cooper, T. Nicolas, and C. Wahlberg, Nucl. Fusion **58**(7), 074001 (2018).
[15] R. Koch, Fusion Sci. Technol. **45**(2T), 183 (2004).
[16] K. Ida, M. Yoshinuma, M. Yokoyama, S. Inagaki, N. Tamura, B. J. Peterson, T. Morisaki, S. Masuzaki, A. Komori, Y. Nagayama, K. Tanaka, K. Narihara, K. Y. Watanabe, C. D. Beidler, and LHD experimental group, Nucl. Fusion **45**(5), 391 (2005).
[17] T. Ii Tsujimura, S. Kubo, H. Takahashi, R. Makino, R. Seki, Y. Yoshimura, H. Igami, T. Shimozuma, K. Ida, C. Suzuki *et al.*, Nucl. Fusion **55**, 123019 (2015).
[18] S. Murakami *et al.*, Trans. Fusion Technol. **27**, 256 (1995).
[19] N. B. Marushchenko, C. D. Beidler, S. V. Kasilov, W. Kernbichler, H. MaaSSberg, R. Prater, and R. W. Harvey, Phys. Plasmas **18**, 032501 (2011).
[20] K. Ida, S. Inagaki, M. Yoshinuma, Y. Narushima, K. Itoh, T. Kobuchi, K. Y. Watanabe, H. Funaba, S. Sakakibara, T. Morisaki, and LHD Experiment Group, Phys. Rev. Lett. **100**, 045003 (2008).
[21] T. Kobayashi, K. Ida, Y. Suzuki, H. Takahashi, Y. Takemura, M. Yoshinuma, H. Tsuchiya, M. Sanders, and LHD Experiment Group, Nucl. Fusion **60**, 036017 (2020).
[22] S. Yamamoto, K. Nagasaki, K. Nagaoka, J. Varela, Á. Cappa, E. Ascasíbar, F. Castejón, J. M. Fontdecaba, J. M. García-Regaña, Á. González-Jerez *et al.*, Nucl. Fusion **60**, 066018 (2020).